Earth and Planetary Science Letters 511 (2019) 190–201

Contents lists available at ScienceDirect

Earth and Planetary Science Letters

www.elsevier.com/locate/epsl

Extreme enriched and heterogeneous $^{87}Sr/^{86}Sr$ ratios recorded in magmatic plagioclase from the Samoan hotspot

M.A. Edwards [a,*], M.G. Jackson [a], A.R.C. Kylander-Clark [a], J. Harvey [b], G.A. Hagen-Peter [c], G.G.E. Seward [a], C.B. Till [d], J.V. Adams [a], J.M. Cottle [a], B.R. Hacker [a], F.J. Spera [a]

[a] Department of Earth Science, University of California Santa Barbara, Santa Barbara, CA 93106, USA
[b] School of Earth and Environment, University of Leeds, Leeds LS2 9JT, UK
[c] Center for Earth System Petrology, Department of Geoscience, Aarhus University, 8000 Aarhus C, Denmark
[d] School of Earth & Space Exploration, Arizona State University, Tempe, AZ 85287, USA

ARTICLE INFO

Article history:
Received 19 September 2018
Received in revised form 20 January 2019
Accepted 23 January 2019
Available online 7 February 2019
Editor: F. Moynier

Keywords:
isotope geochemistry
mantle geochemistry
mantle heterogeneity
LA-ICP-MS
LASS

ABSTRACT

We report the major-element, trace-element, and $^{87}Sr/^{86}Sr$ compositions of six plagioclase crystals from two Samoan lavas with extreme EM2 isotopic compositions (ALIA-115-18 with whole-rock $^{87}Sr/^{86}Sr$ of 0.718592, and ALIA-115-21 with whole-rock $^{87}Sr/^{86}Sr$ of 0.720469). We employed laser-ablation split-stream mass spectrometry (LASS) to simultaneously measure $^{87}Sr/^{86}Sr$ ratios, major-element concentrations, and trace-element concentrations in the same plagioclase crystal volume. We find that two plagioclase crystals have extreme $^{87}Sr/^{86}Sr$ heterogeneity in excess of 5000 ppm (where ppm of $^{87}Sr/^{86}Sr$ variability $= 10^6 \cdot [^{87}Sr/^{86}Sr_{max} - {}^{87}Sr/^{86}Sr_{min}]/^{87}Sr/^{86}Sr_{avg}$). In two of the plagioclase crystals, we identify the highest $^{87}Sr/^{86}Sr$ ratios (0.7224) ever measured in any fresh, mantle-derived ocean island basalt (OIB) or OIB-hosted mineral phase.

We find that in $^{87}Sr/^{86}Sr$-versus-Sr concentration space, the six plagioclase crystals overlap in a "common component" region with higher $^{87}Sr/^{86}Sr$ than has been previously identified in whole-rock Samoan lavas or mineral separates. We use the occurrence of olivine mineral inclusions (Fo $= 74.5 \pm 0.8$, 2 SD) in the high-$^{87}Sr/^{86}Sr$ zone of one plagioclase crystal to infer the bulk composition (Mg# $= 46.8 \pm 0.8$, 2 SD) of the extreme EM2 magma from which the olivine and high-$^{87}Sr/^{86}Sr$ plagioclase crystallized. We argue that a relatively evolved EM2 endmember magma mixed with at least one lower-$^{87}Sr/^{86}Sr$ melt to generate the observed intra-crystal plagioclase isotopic heterogeneity.

By inferring that subducted terrigenous sediment gives rise to EM2 signatures in Samoan lavas, we estimate that the quantity of sediment necessary to generate the most-elevated $^{87}Sr/^{86}Sr$ ratios observed in the Samoan plagioclase is $\sim 7\%$ of the mantle source. We also estimate that sediment subduction into the mantle over geologic time has generated a sediment domain that constitutes 0.02% of the mass of the mantle, a much lower proportion than required in the EM2 mantle source. Even if subducted sediment is concentrated in large low-shear-velocity provinces (LLSVPs) at the base of the mantle (which constitute up to 7.7% of the mantle's mass), then only 0.25% of the LLSVPs are composed of sediment. This requires that the distribution of subducted sediment in the mantle is heterogeneous, and the high relative abundance of sediment in the Samoan EM2 mantle is an anomalous relic of ancient subduction that has survived convective attenuation.

1. Introduction

The observation that ocean island basalts (OIB) show variations in radiogenic isotopic compositions suggests that the mantle is heterogeneous (e.g., Gast et al., 1964; Hart et al., 1973; Zindler and Hart, 1986; Hofmann, 1997; Stracke, 2012; White, 2015). Globally, OIB can be grouped into distinct end-members defined by their Sr, Nd, and Pb isotopic compositions: i) depleted MORB mantle, ii) "high μ" $= {}^{238}U/^{204}Pb$, iii) enriched mantle 1, and iv) enriched mantle 2 (DMM, HIMU, EM1 and EM2, respectively; Zindler and Hart, 1986). Although isotopic differences exist in OIB, the origins, geometries, and ages of the isotopic "domains" in Earth's mantle remain active areas of inquiry.

Studies of mantle-derived lavas most often employ whole-rock isotopic measurements, which homogenize any isotopic heterogeneity that may exist among different phases or within individ-

* Corresponding author.
E-mail address: medwards@ucsb.edu (M.A. Edwards).

https://doi.org/10.1016/j.epsl.2019.01.040
0012-821X/

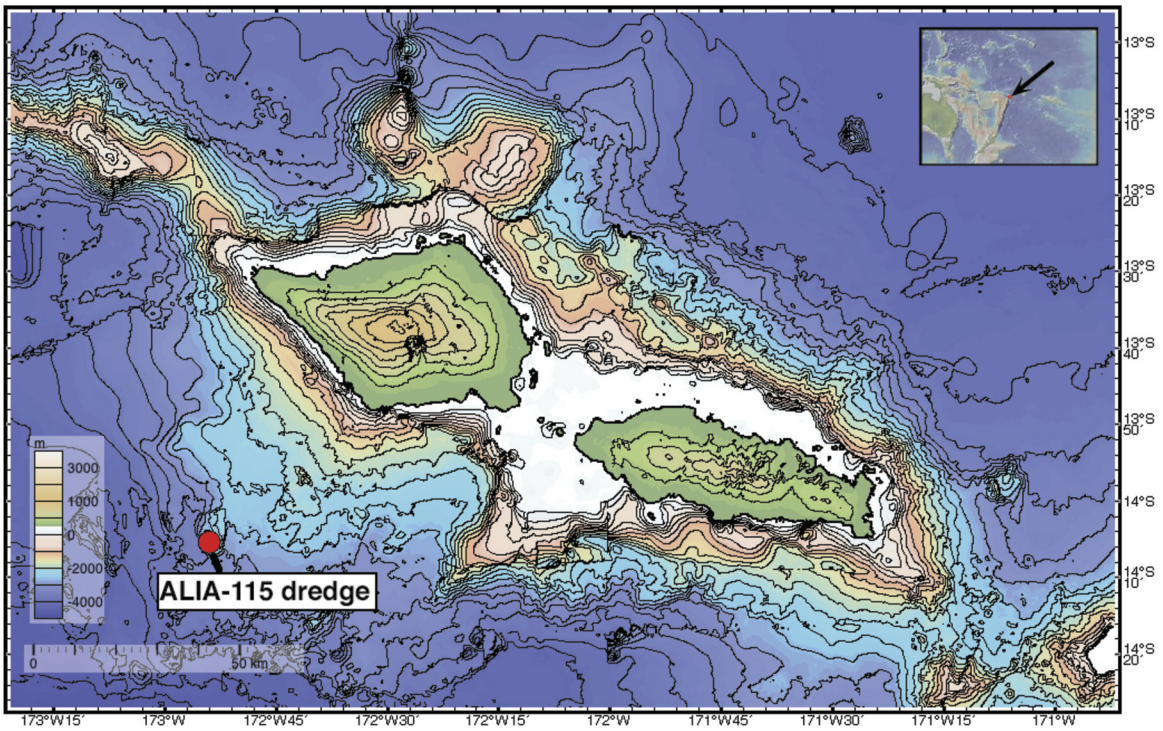

Fig. 1. Map of western Samoa showing the islands of Savai'i (left) and Upolu (right). The inset shows the location of the Samoan chain in the western Pacific. The location of ALIA dredge 115 is indicated (the dredge location is from Jackson et al., 2007). The map was made with GeoMapApp using the GMRT 3.5 DEM. The contour interval is 200 m, and the contour corresponding to an elevation of 0 m is shown in bold.

ual minerals (or melt inclusions) in a lava. Although whole-rock analyses can be useful in identifying large-scale isotopic heterogeneities in Earth's mantle (e.g., Hofmann, 1997; Stracke, 2012; White, 2015), information about possible isotopic heterogeneity within a single lava is lost (e.g., Davidson et al., 2007).

Previous work has identified $^{87}Sr/^{86}Sr$ disequilibrium between olivine-hosted melt inclusions and their host oceanic lavas, an observation that suggests that multiple isotopically distinct melt sources may contribute to a single lava (or that the assimilation of crust modifies the isotopic composition of lavas after olivine crystallization) (e.g., Harlou et al., 2009; Jackson and Hart, 2006; Reinhard et al., 2016; 2018; Sobolev et al., 2011). Lead isotopic variability has also been observed in olivine-hosted melt inclusions in OIB (Saal et al., 1998; Yurimoto et al., 2004; Sobolev et al., 2011), although the extent of this variability has been debated (Paul et al., 2011). Furthermore, the Sr, Nd, and Pb isotopic compositions of clinopyroxene hosted in OIB lavas have been demonstrated to be in isotopic disequilibrium with their host whole rocks (Hanyu and Nakamura, 2000; Jackson et al., 2009; Hanyu et al., 2011; Miyazaki et al., 2018). These studies collectively suggest that intra-lava isotopic heterogeneity exists in some OIB. However, the mechanisms for generating this heterogeneity remain unresolved.

Plagioclase is well suited to evaluating the nature and origin of $^{87}Sr/^{86}Sr$ heterogeneity in OIB lavas because i) Sr is compatible in plagioclase, so plagioclase has elevated Sr concentrations relative to the bulk rock; ii) plagioclase has low Rb concentrations, thereby minimizing the impact of the isobaric interference of ^{87}Rb on mass 87 when employing in situ analytical methods; iii) plagioclase can contain domains (or zones) with distinct $^{87}Sr/^{86}Sr$ compositions (Christensen et al., 1995; Davidson and Tepley, 1997; Ramos et al., 2005; Font et al., 2008; Lange et al., 2013); and iv) $^{87}Sr/^{86}Sr$ compositions can be linked to the major- and trace-element compositional domains in the plagioclase. Such domains record a "crystal stratigraphy" that can provide relative temporal information (from plagioclase core to rim) about the processes that contributed to the isotopic composition of a single plagioclase crystal.

To our knowledge, intra-crystal $^{87}Sr/^{86}Sr$ zonation has not been reported in plagioclase in OIB. Therefore, this study uses LASS (laser-ablation split-stream mass spectrometry; Kylander-Clark et al., 2013) to measure the $^{87}Sr/^{86}Sr$ and major- and trace-element compositions of six plagioclase crystals hosted in two extreme EM2 lavas from the Samoan hotspot with the most elevated $^{87}Sr/^{86}Sr$ signatures ever reported in global OIB (with whole-rock $^{87}Sr/^{86}Sr$ of 0.718592 and 0.720469; Jackson et al., 2007).

2. Sample description and methods

2.1. Sample description and EPMA analysis

We targeted two lavas from the Samoan hotspot—ALIA-115-18 and ALIA-115-21—that have previously been characterized for whole-rock isotopic, major-element, and trace-element geochemistry. ALIA-115-18 and ALIA-115-21—a trachybasalt and trachyandesite, respectively—were dredged aboard the R/V Kilo Moana in April 2005 from the deep (3220 m below sea level) southwest flank of Savai'i Island, western Samoa (Fig. 1) (Jackson et al., 2007; Koppers et al., 2008). A suite of five rocks from ALIA dredge 115 range in age from 4.98 to 5.06 Ma (Koppers et al., 2008). ALIA-115-18 (whole-rock $^{87}Sr/^{86}Sr$ is 0.718592) and ALIA-115-21 (whole-rock $^{87}Sr/^{86}Sr$ is 0.720469; Jackson et al., 2007) have the most geochemically enriched $^{87}Sr/^{86}Sr$ signatures measured in whole-rock OIB to date (Fig. 2). Previous work on samples ALIA-115-18 and ALIA-115-21 also revealed significant $^{87}Sr/^{86}Sr$ disequilibrium (up to 3115 ppm and 1611 ppm, respectively) between clinopyroxene and the host whole rocks (Jackson et al., 2009), making these two samples ideal targets for investigating $^{87}Sr/^{86}Sr$ heterogeneity in OIB-hosted plagioclase. ALIA-115-18 and ALIA-115-21 host large, mm-scale plagioclase crystals (see electron probe microanalysis [EPMA] images in Supplementary Fig. 1)

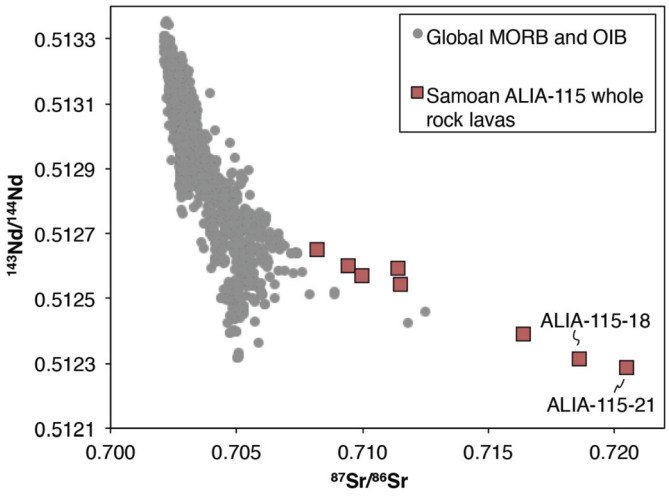

Fig. 2. Global ocean island basalt and mid-ocean ridge basalt isotopic array ("mantle array") in $^{143}Nd/^{144}Nd$–$^{87}Sr/^{86}Sr$ space. Data are from the compilation of Stracke et al. (2003), with additional Samoan isotopic data from Workman et al. (2004) and Jackson et al. (2007). ALIA dredge 115 lavas are shown in red, with ALIA-115-18 and ALIA-115-21 whole rocks annotated. We investigate the compositions of plagioclase crystals from these two whole rock lavas in this study. (For interpretation of the colors in this and subsequent figures, the reader is referred to the web version of this article.)

that were targeted here. See the Supplementary Methods for a description of sample preparation, EPMA mapping of the plagioclase crystals, and EPMA analysis of olivine inclusions in plagioclase ALIA-115-18-1 (Table 1).

2.2. Laser ablation split-stream mass spectrometry

We employed LASS to simultaneously measure major- and trace-element concentrations and $^{87}Sr/^{86}Sr$ compositions of Samoan plagioclase. This analytical approach couples a Teledyne CETAC Photon Machines *Analyte* 193 nm ArF excimer laser and HelEx sample cell to two mass spectrometers: a Nu Instruments *Plasma HR* multi-collector inductively coupled plasma mass spectrometer (MC-ICP-MS) for $^{87}Sr/^{86}Sr$ measurements, and an Agilent 7700*X* quadrupole inductively coupled plasma mass spectrometer (Q-ICP-MS) for trace-element concentration measurements. The ablated sample is mixed in a mixing bulb; the sample flow path is then split such that approximately half of the sample is directed to each mass spectrometer. The LASS facility at the University of California at Santa Barbara is described in detail by Kylander-Clark et al. (2013).

LASS enables investigation of the relationships between $^{87}Sr/^{86}Sr$ and plagioclase major- and trace-element geochemistry from the same laser spot, and thereby facilitates the interpretation of isotopic data. Additionally, LASS allows filtering or discarding of $^{87}Sr/^{86}Sr$ analyses that contain inclusions or other phases. As a result, LASS allows targeting of phase-specific $^{87}Sr/^{86}Sr$ data by identifying and discarding isotopic data associated with non-plagioclase trace-element signatures (Fig. 3). For each ALIA-115 plagioclase crystal, data from multiple spot analyses on each crystal were used to generate model $^{87}Sr/^{86}Sr$ and Sr concentration surfaces using Matlab® (Fig. 4 and Supplementary Fig. 2).

2.2.1. LASS $^{87}Sr/^{86}Sr$ measurements

The $^{87}Sr/^{86}Sr$ composition of plagioclase can be measured using LA-MC-ICP-MS with sufficient precision to resolve isotopic variability, though complicating factors include instrumental mass fractionation and isobaric interferences (Davidson et al., 2007). In practice, mass fractionation can be corrected by monitoring deviations from a canonical $^{86}Sr/^{88}Sr$ stable isotope ratio (0.1194) and cor-

Table 1
Compositions of four olivines included in plagioclase ALIA-115-18-1.

	Number of spot analyses	SiO_2 (wt%)	2σ	MgO (wt%)	2σ	FeO (wt%)	2σ	NiO (wt%)	2σ	MnO (wt%)	2σ	Al_2O_3 (wt%)	2σ	Cr_2O_3 (wt%)	2σ	CaO (wt%)	2σ	Total (wt%)	Fo#	2σ
Olivine 1	5	37.76	0.42	37.38	0.40	22.98	0.12	0.11	0.01	0.31	0.01	0.02	0.01	0.01	0.02	0.28	0.02	98.86	74.36	0.27
Olivine 2	3	39.22	1.10	38.79	1.05	22.95	0.01	0.11	0.00	0.31	0.01	0.03	0.02	0.00	0.01	0.31	0.02	101.72	75.08	0.50
Olivine 3	5	37.68	0.25	37.15	0.29	23.07	0.09	0.11	0.01	0.31	0.01	0.03	0.01	0.01	0.01	0.28	0.01	98.63	74.17	0.12
Olivine 4	1	37.61	n/a	37.05	n/a	22.61	n/a	0.10	n/a	0.31	n/a	0.05	n/a	0.00	n/a	0.37	n/a	98.10	74.50	n/a

Four olivines included in a zone in the ALIA-115-18-1 plagioclase crystal were analyzed by EPMA as described in the text. Each olivine was analyzed at between 1 to 5 separate spot locations. The 2 SD reproducibility of each oxide and of the calculated Fo# of olivines that were analyzed multiple times are reported.

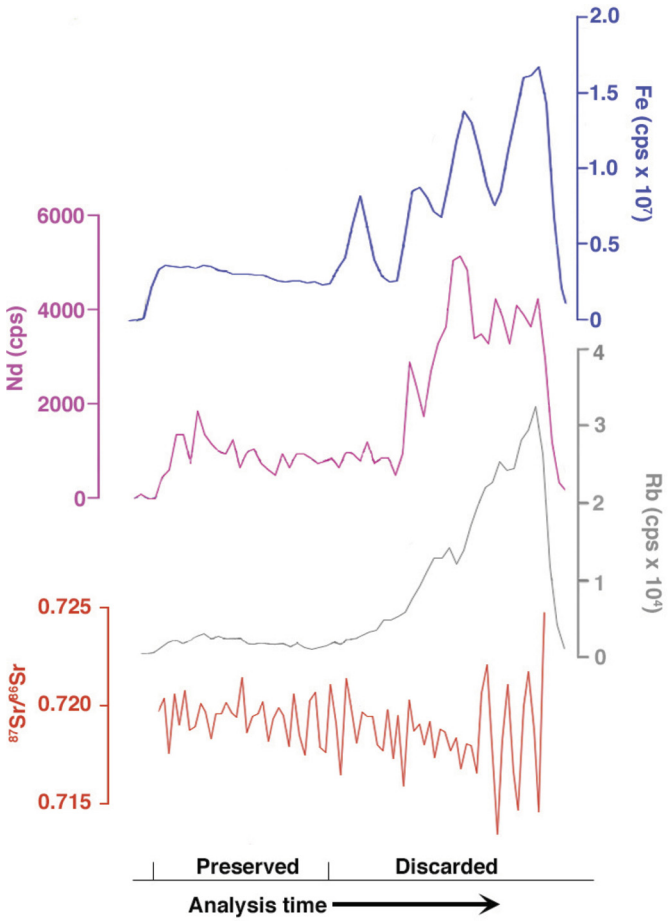

Fig. 3. Demonstration of the utility of LASS for generating plagioclase-specific Sr isotopic data. In this analysis (spot 51 from crystal ALIA-115-18-2 in Supplementary Table 4), an inclusion of unknown affinity is encountered during the latter portion of the analysis. The inclusion is characterized by elevated Fe, REE (Nd is shown as an example), and Rb concentrations. The $^{87}Sr/^{86}Sr$ ratio is impacted by this inclusion, but simultaneous collection of major- and trace-element data via LASS allows us to reject the inclusion-influenced data. The figure shows counts per second (cps) for each element rather than concentration (in ppm) because the ^{43}Ca concentration used as an internal standard is not the same in the plagioclase and the inclusion.

recting the measured $^{87}Sr/^{86}Sr$ ratio using the exponential mass fractionation law. However, isobaric interferences on mass 86 from ^{86}Kr (present as a contaminant in the Ar carrier gas) can result in inaccurate measured $^{86}Sr/^{88}Sr$ and $^{87}Sr/^{86}Sr$ ratios. Therefore, in this study the Kr correction approach described by Konter and Storm (2014) was implemented to correct for Kr interferences. For a detailed description of this correction algorithm and of the MC-ICP-MS analytical procedures employed in this study, refer to Konter and Storm (2014) and the Supplementary Methods.

After correction for isobaric interferences (Kr and Rb; see Supplementary Methods) and mass fractionation, we used an in-house plagioclase primary reference material to correct the measured $^{87}Sr/^{86}Sr$ ratios of samples and secondary reference materials. This primary reference material, T21 (a homogenized plagioclase glass), was prepared by separating 450 mg of inclusion-free plagioclase chips from plagioclase-rich Samoan basalt sample T21 (see Workman et al., 2004). The plagioclase chips were powdered to < 40 µm and fused twice in a 1500 °C furnace at Arizona State University, resulting in a homogeneous plagioclase glass (see Supplementary Table 1 for the major-element composition and Supplementary Table 2 for the trace-element composition of T21). The $^{87}Sr/^{86}Sr$ value of T21—determined via TIMS at the University of Leeds and corrected to an NBS987 $^{87}Sr/^{86}Sr$ value of 0.710240—is 0.704712 ±0.000009 (2 SE) (see Table 2), similar to the whole-rock $^{87}Sr/^{86}Sr$ value of T21 (0.704751; Workman et al., 2004). The offset between the preferred TIMS and measured LASS $^{87}Sr/^{86}Sr$ values for T21 is calculated, and this offset (or "correction factor") is applied to all secondary reference materials and plagioclase samples using a linear interpolation. Following application of the correction factor, the secondary reference materials measured during the course of this study yield accurate $^{87}Sr/^{86}Sr$ ratios (see below).

Secondary reference materials for $^{87}Sr/^{86}Sr$ used in this study include a naturally homogeneous plagioclase crystal from the American Museum of Natural History, AMNH 107160 plagioclase ($^{87}Sr/^{86}Sr = 0.704386 \pm 0.000008$ [2 SE] via TIMS, Table 2; see Supplementary Table 1 for major-element analyses and Supplementary Table 2 for trace-element analyses), the USGS MACS-3 carbonate reference material ($^{87}Sr/^{86}Sr = 0.707546 \pm 0.000004$ [2 SE] via TIMS; Jochum et al., 2011), and a modern sclerosponge ($^{87}Sr/^{86}Sr$ of modern seawater $= 0.709164 \pm 0.000002$ [2 SE] via TIMS; Mokadem et al., 2015). All $^{87}Sr/^{86}Sr$ values of the primary and secondary reference materials have been normalized to an NBS987 $^{87}Sr/^{86}Sr$ value of 0.710240.

LASS analyses were conducted during three analytical sessions on 3/2/2017, 5/8/2017, and 8/15/2017. A summary of all LASS and

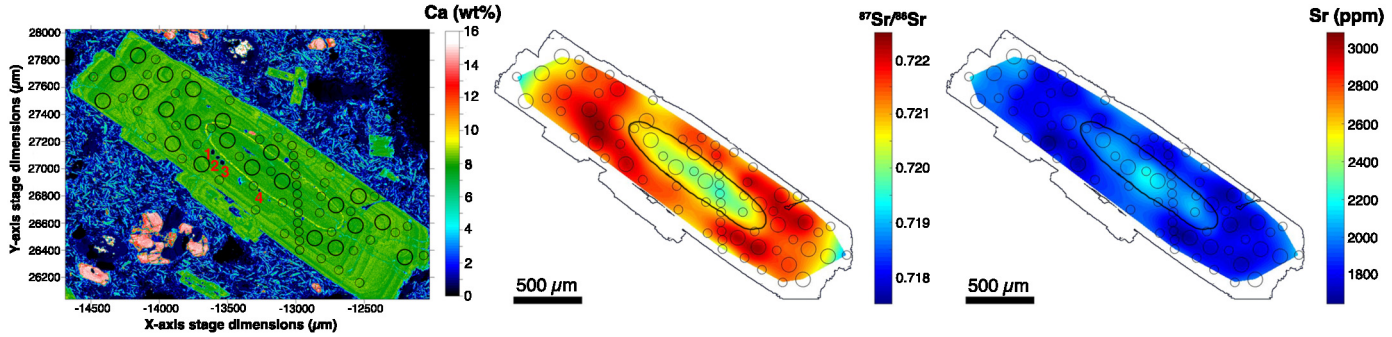

Fig. 4. Quantitative Ca concentration map (left), $^{87}Sr/^{86}Sr$ model surface (middle), and Sr concentration model surface (right) for plagioclase ALIA-115-18-1. The Ca EPMA map was produced using Probe for EPMA and CalcImage (Probe Software, Inc.), and the $^{87}Sr/^{86}Sr$ and Sr concentration surfaces were generated using Matlab® (see Supplementary Methods). In each image, the location of the laser spots is indicated by circles with sizes corresponding to the laser spot size (see Supplementary Fig. 1 for the Ca map with laser spot numbers added). The four olivine inclusions measured by EPMA spot analyses are indicated with red numbers in the EPMA image (see Table 1 for the olivine compositions). The olivines occur just outside of the rounded and resorbed core within a zone referred to in the text as the "olivine-bearing zone", which corresponds to high $^{87}Sr/^{86}Sr$ (and thus the plagioclase in this olivine-bearing zone samples the extreme EM2 "common component" shown in Fig. 6). The boundary between the core and the rest of the crystal (the "core-mantle boundary") is visible as an irregular yellow line (owing to elevated Ca concentration) in the left panel. Lines indicating the crystal's edge and the "core-mantle boundary" are drawn on the model surfaces in the middle and right panels. Analogous figures for the other five Samoan plagioclase crystals from this study are shown in Supplementary Fig. 2, and EPMA elemental maps for other major elements (Si, Al, Na, etc.) are shown in Supplementary Fig. 1.

Table 2
New TIMS analyses of reference materials in this study.

Sample name	Sample type	Estimated Sr[a] (ng)	TIMS $^{87}Sr/^{86}Sr$[b]	2 SE	LA-MC-ICP-MS $^{87}Sr/^{86}Sr$[c]	2 SD
Analyses conducted October 2015						
NBS987	Solution	–	0.710247	0.000015	–	–
BHVO-1	Powder	–	0.703503	0.000004	–	–
T21 homogenized plagioclase	Mineral fragment	–	0.704712	0.000009	–	–
Analyses conducted October 2017						
NBS987	Solution	–	0.710233	0.000014	–	–
BHVO-2	Powder	–	0.703470	0.000012	–	–
T21 homogenized plagioclase	Micromilled powder	18	0.704699	0.000018	–	–
AMNH 107160 plagioclase	Mineral fragment	–	0.704386	0.000008	0.70436	0.00026
AMNH 107160 plagioclase	Micromilled powder	15	0.704408	0.000020	0.70436	0.00026
Pit-16 plagioclase	Micromilled powder	49	0.704505	0.000012	0.70442	0.00018

[a] Sr quantities for micromilled powders are estimated from the milled volume and the measured Sr concentration of each plagioclase (see Supplementary Table 2), and assume 100% recovery and a plagioclase density of 2.7 g/cm^3.
[b] Aside from NBS987, all reported $^{87}Sr/^{86}Sr$ values are normalized to NBS987 $^{87}Sr/^{86}Sr = 0.710240$.
[c] LA-MC-ICP-MS values are averages of multiple analyses over the course of this study, which are summarized in Table 3 and reported in Supplementary Table 3.

Table 3
$^{87}Sr/^{86}Sr$ values measured from geological reference materials by LA-MC-ICP-MS in this study compared to TIMS reference values.

Reference material	Mean measured $^{87}Sr/^{86}Sr$ by LA-MC-ICP-MS[a]	LA-MC-ICP-MS 2 SD	LA-MC-ICP-MS 2 SD (ppm)	Number of analyses	TIMS reference $^{87}Sr/^{86}Sr$[b]	TIMS reference uncertainty[c]	Difference between LA-MC-ICP-MS and TIMS reference values (ppm)
AMNH 107160 plagioclase	0.70436	0.00026	363	73	0.704386	0.000008 (2SE)	−33
Pit-16 plagioclase	0.70442	0.00018	257	19	0.704505	0.000012 (2SE)	−115
USGS MACS-3 carbonate	0.70754	0.00019	270	40	0.707546	0.000004 (2SD, $n = 5$)	−6
Modern sclerosponge	0.70916	0.00018	260	40	0.709164	0.000002 (2SD, $n = 17$)	1

[a] Refer to Supplementary Table 3 for the individual analyses used to calculate the mean measured Sr isotopic composition and uncertainties reported here.
[b] The reference values for AMNH 107160 plagioclase and Pit-16 plagioclase were obtained by TIMS and are reported in Table 2. The USGS MACS-3 carbonate reference value is reported in Jochum et al. (2011). The reference value for the modern sclerosponge is the modern seawater value of Mokadem et al. (2015). All reference and measured values have been normalized to NBS987 $^{87}Sr/^{86}Sr = 0.710240$.
[c] Reference value analytical uncertainties for AMNH 107160 and Pit-16 plagioclase are 2 SE. Uncertainties for MACS-3 and modern sclerosponge—for which reference values are means of multiple ratios—are 2 SD.

TIMS $^{87}Sr/^{86}Sr$ analyses of secondary materials—as well as analyses of an OIB-hosted plagioclase with homogeneous $^{87}Sr/^{86}Sr$ from Pitcairn sample Pit-16 (Garapić et al., 2015; see Supplementary Methods)—is available in Table 3, and $^{87}Sr/^{86}Sr$ (and major- and trace-element) data from each laser spot are available in Supplementary Table 3. Following correction to the preferred T21 value, the mean $^{87}Sr/^{86}Sr$ values of the three secondary $^{87}Sr/^{86}Sr$ reference materials (AMNH 107160 plagioclase, USGS MACS-3 carbonate, and modern sclerosponge) obtained by LASS—AMNH 107160, MACS-3, and the sclerosponge—agree with the TIMS reference values to better than 33 ppm. Additionally, the reproducibility of measured $^{87}Sr/^{86}Sr$ was ±260 ppm (2 RSD, $n = 40$) for the modern sclerosponge over three analytical sessions, ±270 ppm (2 RSD, $n = 40$) for MACS-3 over three analytical sessions, and ±353 ppm (2 RSD, $n = 73$) for AMNH 107160 plagioclase over two analytical sessions. The mean $^{87}Sr/^{86}Sr$ value measured by LASS for Pit-16 plagioclase agrees with the value measured for the micromilled powder measured via TIMS within 115 ppm (see Table 3, Supplementary Fig. 3, and Supplementary Methods). Reference materials and samples were analyzed identically aside from the laser spot size and repetition rate, which we varied according to the Sr concentration of the analyte. The T21 primary reference material (1306 ppm Sr; Supplementary Table 2) and the AMNH 107160 secondary reference material (968 ppm) have lower Sr concentrations than the ALIA-115-18 (2054 ± 461 ppm, 2 SD; Supplementary Table 4) and the ALIA-115-21 (2218 ± 656 ppm, 2 SD) plagioclase crystals. During the analytical sessions, we analyzed the T21 and AMNH 107160 plagioclase reference materials every fourth sample analysis, and the MACS-3 and sclerosponge reference materials every twentieth sample analysis.

2.2.2. LASS major- and trace-element measurements

We measured the major- and trace-element compositions of plagioclase by LASS. A detailed description of LASS trace-element measurement procedures and the accuracy and reproducibility of LASS major- and trace-element measurements of reference materials is in the Supplementary Methods. Major- and trace-element concentrations obtained by LASS used ^{43}Ca as an internal standard. For T21 plagioclase, AMNH 107160 plagioclase, Pit-16 plagioclase, and all Samoan plagioclase crystals analyzed by LASS in this study, ^{43}Ca is from EPMA Ca concentration measurements (Supplementary Tables 2–4).

3. Data and observations

We targeted six individual plagioclase crystals from Samoan lava samples ALIA-115-18 and ALIA-115-21. A summary of all $^{87}Sr/^{86}Sr$, trace-element, and major-element geochemical data obtained from these plagioclase crystals is in Supplementary Table 4. All $^{87}Sr/^{86}Sr$ measurements are summarized in Fig. 5, and plagioclase $^{87}Sr/^{86}Sr$ results are compared to whole-rock and clinopyroxene $^{87}Sr/^{86}Sr$ values previously obtained from samples ALIA-115-18 and ALIA-115-21 (Jackson et al., 2007; 2009). We identify plagioclase domains with $^{87}Sr/^{86}Sr$ compositions that extend to values both lower and higher than those identified in host whole rocks and in clinopyroxene from the same lavas (Fig. 5). We find significant intra-crystal isotopic heterogeneity in most of the plagioclase crystals that in some cases greatly exceeds the analytical reproducibility of LASS $^{87}Sr/^{86}Sr$ measurements of reference materials.

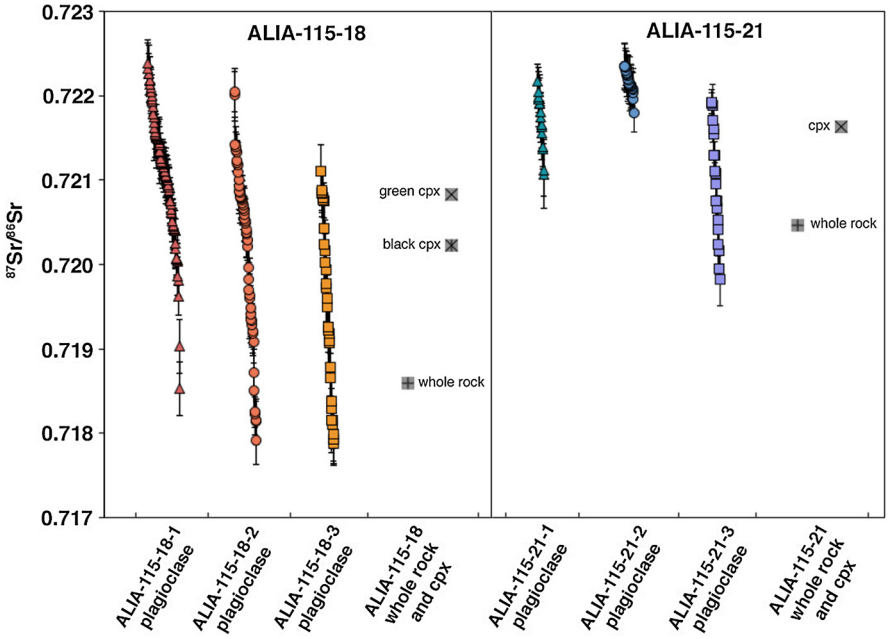

Fig. 5. LASS $^{87}Sr/^{86}Sr$ data from the six Samoan plagioclase targeted in this study (see Supplementary Table 4 for the $^{87}Sr/^{86}Sr$ values and uncertainties used to make the figure). Error bars are internal 2 SE. Whole-rock (Jackson et al., 2007) and cpx (Jackson et al., 2009) values from each lava (shown as squares) are plotted adjacent to the respective plagioclase data.

3.1. Description of individual crystals and geochemical characteristics

3.1.1. ALIA-115-18 plagioclase

The three plagioclase crystals from Samoan lava ALIA-115-18 targeted here are approximately 2 mm × 0.5 mm in size and are characterized by the presence of fine oscillatory zoning that is visible in the quantitative EPMA maps of each grain (Supplementary Fig. 1). The morphology and geochemical data collected for individual plagioclase crystals from ALIA-115-18 are described below.

ALIA-115-18-1: This plagioclase has a rounded, resorbed core with olivine and clinopyroxene inclusions along the outer edge of the core (see Supplementary Fig. 1 for EPMA maps of this crystal). The average anorthite content (An = molar Ca/[Ca + Na] · 100) of this crystal at locations corresponding to each of the laser spots is 59 ± 2 (2 SD, using EPMA data compiled in Supplementary Table 4). We measured the $^{87}Sr/^{86}Sr$ and trace-element composition of this plagioclase in 75 spot locations over three analytical sessions. This plagioclase exhibits coherent $^{87}Sr/^{86}Sr$ zoning: a low-$^{87}Sr/^{86}Sr$ core is surrounded by a high-$^{87}Sr/^{86}Sr$ mantle, and a thin (c. 100 μm) low-$^{87}Sr/^{86}Sr$ rim (Fig. 4). Small (c. 20–30 μm) olivine inclusions occur in the plagioclase within the high-$^{87}Sr/^{86}Sr$ zone—called the "olivine-bearing zone" hereafter—near the boundary with the low $^{87}Sr/^{86}Sr$ core (Fig. 4). The $^{87}Sr/^{86}Sr$ values measured in this plagioclase span from 0.71853 ± 0.00032 (2 SE) to 0.72239 ± 0.00027 (2 SE); the measured $^{87}Sr/^{86}Sr$ range is approximately 5300 ppm. As with the other plagioclase crystals in this study, Sr concentration shows an inverse relationship with $^{87}Sr/^{86}Sr$ (see section 3.2 and Fig. 6). This anticorrelation is also demonstrated in Fig. 4, wherein the low-$^{87}Sr/^{86}Sr$ core has elevated Sr concentrations, and the high-$^{87}Sr/^{86}Sr$ region has lower Sr concentrations.

The mean $^{87}Sr/^{86}Sr$ value of four analyses made from the olivine-bearing zone is 0.72194 ± 0.00057 (2 SE), indistinguishable from (i.e., within uncertainty of) the highest value (0.72239 ± 0.00027 [2 SE]; Supplementary Table 4) reported in this study. We targeted four olivine inclusions with EPMA spot analyses (see Table 1) in order to calculate the equilibrium melt Mg# associated with the olivines. The analyzed olivines have a mean forsterite content (= molar Mg/[Mg + Fe^{2+}] · 100) of 74.5 ± 0.8 (2 SD, n = 14 measurements from 4 different olivine inclusions). Assuming an olivine-melt K_D of 0.3 (where $K_D = [Fe^{2+}/Mg]_{olivine}/[Fe^{2+}/Mg]_{melt}$; Roeder and Emslie, 1970), this olivine was in equilibrium with a melt with Mg# = 46.8 ± 0.4 (2 SD) (where Mg# is molar Mg/[Mg + Fe^{2+}] · 100). An uncertainty of 10% in the K_D value yields a range in calculated equilibrium Mg# of 44 to 49, which is depicted by the error bars shown in Fig. 7.

ALIA-115-18-2: Plagioclase ALIA-115-18-2 contains multiple isolated regions of concentric anorthite zoning surrounded by a rim (Supplementary Fig. 1). The mean An content of this crystal is 59 ± 3 (2 SD) at the location of the laser spots (see data in Supplementary Table 4). We measured the $^{87}Sr/^{86}Sr$ composition of this plagioclase in 52 spot locations over two analytical sessions on 5/7/2017 and 8/15/2017. EPMA elemental maps of this sample were generated after the first (but before the second) laser ablation analytical session; therefore, we used the mean Ca concentration from the locations of the laser spots from the second analytical session as an internal standard to calculate trace-element concentrations from the first laser-ablation analytical session. Because the Ca concentration for this crystal varies by only 11% (2 RSD; the Ca content at the locations of the laser spots is 8.12 ± 0.45 wt%, 2 SD, n = 40), this approximation introduces minimal additional uncertainty to the measured trace-element concentrations. The range (5700 ppm) in $^{87}Sr/^{86}Sr$ values measured in this plagioclase (0.71792 ± 0.00028 [2 SE] to 0.72205 ± 0.00024 [2 SE]) is greater than that measured in any of the other plagioclase crystals in this study. This crystal has a core characterized by low $^{87}Sr/^{86}Sr$, a mantle with moderate $^{87}Sr/^{86}Sr$, and a rim with high $^{87}Sr/^{86}Sr$ (Supplementary Fig. 2).

ALIA-115-18-3: Plagioclase crystal ALIA-115-18-3 has an irregular core surrounded by a region characterized by oscillatory major-element zoning (Supplementary Fig. 1). The An content of this crystal is 58 ± 3 (2 SD, n = 31) determined at the location of each of the laser spots (Supplementary Table 4), which is similar to the preceding two ALIA-115-18 plagioclase crystals. We measured the $^{87}Sr/^{86}Sr$ and trace-element composition of this crystal in 30 locations over two analytical sessions. The measured $^{87}Sr/^{86}Sr$ values in this sample span 0.71789 ± 0.00024 (2 SE)

to 0.72111 ± 0.00031 (2 SE); the measured range of $^{87}Sr/^{86}Sr$ is approximately 4400 ppm. This crystal has the lowest measured $^{87}Sr/^{86}Sr$ in this study (0.71789), but no measured $^{87}Sr/^{86}Sr$ values as high as those observed in the other two ALIA-115-18 plagioclase crystals (Fig. 5). In contrast to the two previously described crystals from ALIA-115-18, this crystal contains a core characterized by high $^{87}Sr/^{86}Sr$ that is surrounded by a mantle with lower $^{87}Sr/^{86}Sr$.

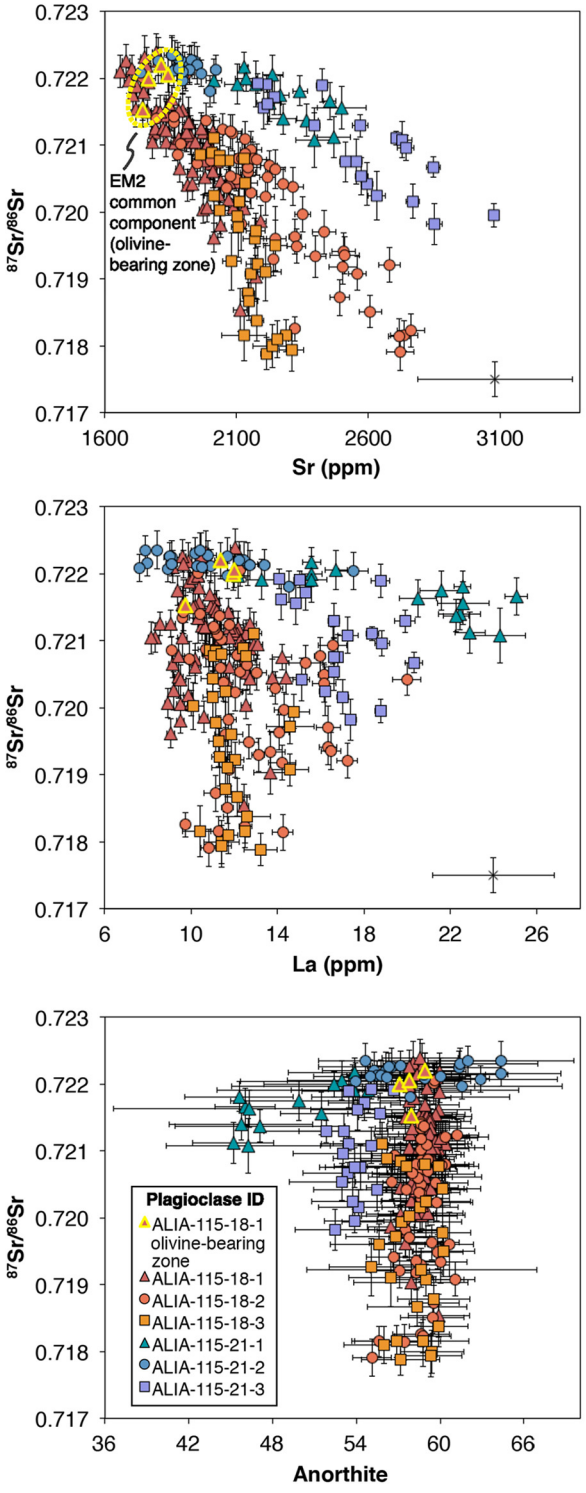

Fig. 6. Samoan plagioclase data from this study plotted in $^{87}Sr/^{86}Sr$–Sr space (top panel), $^{87}Sr/^{86}Sr$–La concentration space (middle panel), and $^{87}Sr/^{86}Sr$–anorthite space (lower panel). The four analyses from the olivine-bearing zone in plagioclase ALIA-115-18-1 are shown with yellow outlines. We selected the "olivine-bearing zone" plagioclase analyses by choosing laser spots from the zone nearest the olivine inclusions. We avoided laser spots that overlap with or contact the resorption surface itself because these analyses capture both the high-$^{87}Sr/^{86}Sr$ zone of the crystal and the low-$^{87}Sr/^{86}Sr$ core (and thus only four laser spot analyses are used to define the $^{87}Sr/^{86}Sr$ of the olivine zone). The four analyses from the olivine-bearing zone are circled in the top panel with a dashed yellow line, and the region encompassed by the yellow oval corresponds with the common region of overlap between the plagioclase crystals from ALIA-115-18 and the crystals form ALIA-115-21. $^{87}Sr/^{86}Sr$, Sr, and La error bars on the datapoints are internal 2 SE. Error bars for the long-term reproducibility of $^{87}Sr/^{86}Sr$ (±363 ppm, 2 SD, for plagioclase reference material AMNH 107160, $n = 73$ analyses; Supplementary Table 3), Sr (±9.5%, 2 SD, for plagioclase reference material T21, $n = 95$ analyses; Supplementary Table 3) and La (±11.7%, 2 SD, for plagioclase reference material T21, $n = 95$ analyses; Supplementary Table 3) are shown in the lower right portion of the top two panels. Anorthite (An = molar Ca/[Ca + Na] · 100) compositions are averages calculated from quantitative EPMA maps of each plagioclase crystal (see Supplementary Fig. 1 for EPMA maps). The anorthite error bars are calculated by propagating one standard deviation of the Na and Ca measurements at the location of each laser spot. All data shown in the figure are reported in Supplementary Table 4.

3.1.2. ALIA-115-21 plagioclase

We measured the $^{87}Sr/^{86}Sr$, major-element, and trace-element composition of three plagioclase crystals from Samoan lava ALIA-115-21, and found that the crystals exhibit more variability in An content (both higher and lower An values) than the ALIA-115-18 crystals (see lower panel of Fig. 6). Additionally, although the ALIA-115-21 crystals extend to $^{87}Sr/^{86}Sr$ values as high as those observed in plagioclase from ALIA-115-18, the ALIA-115-21 plagioclase do not extend to the low $^{87}Sr/^{86}Sr$ values observed in the ALIA-115-18 crystals. Compared to ALIA-115-18 plagioclase, a greater proportion of ALIA-115-21 LASS analyses revealed the presence of non-plagioclase inclusions or cracks; nonetheless, LASS enabled us to reject or trim such analyses (e.g., Fig. 3).

ALIA-115-21-1: This plagioclase is 1.5 mm × 0.3 mm in size. This crystal has a large, Ca-rich core (An as high as 54) surrounded by a Na-rich rim (An as low as 45). The mean An content from the laser spots is 50 ± 7 (2 SD; see Supplementary Table 4), which is quite variable and lower than the other plagioclase crystals examined in this study (Fig. 6). The $^{87}Sr/^{86}Sr$ ratios in this plagioclase, determined in 15 locations over two analytical sessions, extend from 0.72078 ± 0.00028 (2 SE) to 0.72232 ± 0.00021 (2 SE) (range > 2100 ppm).

ALIA-115-21-2: Plagioclase ALIA-115-21-2 is a glomerocryst of three individual plagioclase crystals; additional, smaller crystals are present, but were not analyzed. Two of the three large crystals have notably Ca-rich cores (see Ca EPMA map in Supplementary Fig. 1). This glomerocryst has the highest anorthite content of any plagioclase targeted here (64), with an average An content of 58 ± 6 (2 SD, $n = 23$) from the locations of the laser spots (Fig. 6; Supplementary Table 4). Of all of the Samoan plagioclase evaluated here, ALIA-115-21-2 has the least isotopic variability (Fig. 5). The mean $^{87}Sr/^{86}Sr$ of this plagioclase is 0.72216 ± 0.00026 (2 SD, $n = 23$ spots), and $^{87}Sr/^{86}Sr$ ranges from 0.72180 ± 0.00023 (2 SE) to 0.72235 ± 0.00028 (2 SE), determined in 23 locations over two analytical sessions. At 762 ppm, the range of measured $^{87}Sr/^{86}Sr$ values is approximately twice the 2 SD reproducibility achieved for the AMNH 107160 plagioclase reference material.

ALIA-115-21-3: Plagioclase ALIA-115-21-3 is a glomerocryst consisting of a larger crystal intergrown with at least two smaller crystals. The glomerocryst is approximately 2 mm × 0.5 mm in size. Each sub-crystal exhibits major-element zoning (see Supplementary Fig. 1), but the anorthite content calculated at the location of each laser spot in this plagioclase shows limited variability

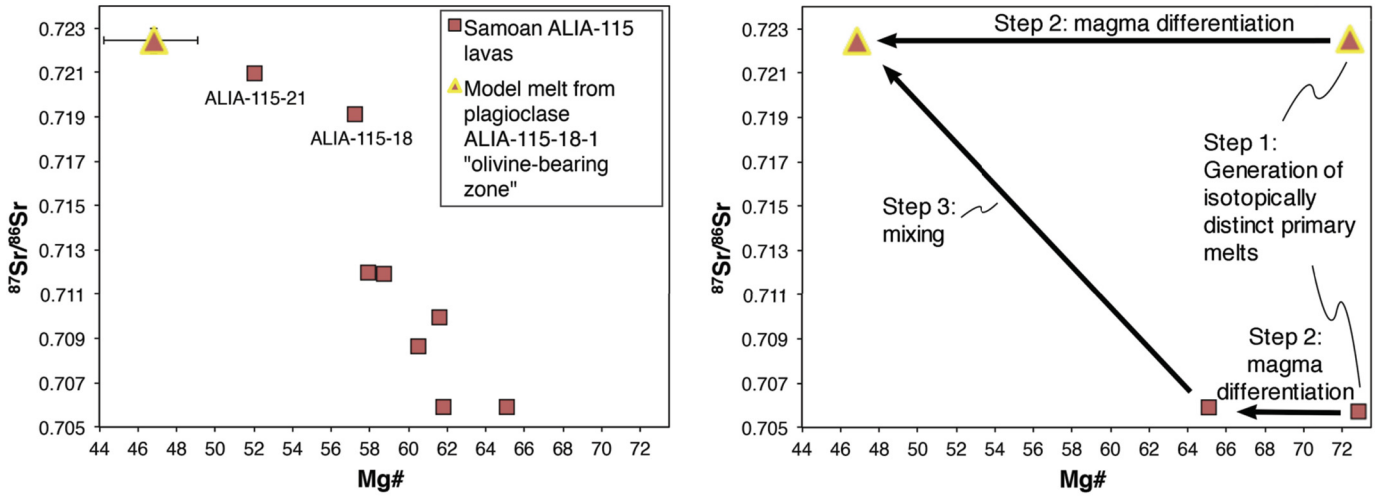

Fig. 7. Left panel: $^{87}Sr/^{86}Sr$ plotted against Mg# of ALIA dredge 115 whole-rock lavas. A red triangle (with yellow outline) representing the olivine-bearing zone from plagioclase ALIA-115-18-1 is also plotted: the $^{87}Sr/^{86}Sr$ value for the olivine-bearing zone from ALIA-115-18-1 is the mean measured $^{87}Sr/^{86}Sr$ value (0.72194 ± 0.00057, 2 SD) of four laser spots (numbers 29, 48, 57, and 73; see Supplementary Table 4) near the olivine-bearing zone in this crystal that target the high-$^{87}Sr/^{86}Sr$ zone with the olivine inclusions; the Mg# (46.8 ± 0.4, 2 SD) shown for the olivine-bearing zone is a melt calculated to be in equilibrium with the average forsterite content (74.5 ± 0.8, 2 SD) measured by EPMA in four olivine inclusions (see Table 1 for olivine compositions and Fig. 4 for an image of ALIA-115-18-1 with the olivine locations annotated). The Mg# calculation assumes an olivine-melt Fe–Mg K_D of 0.30 ± 0.03 (Roeder and Emslie, 1970). The Mg# error bars represent 10% uncertainty in the partition coefficient. The Mg# shown for whole-rock lavas assumes that 90% of total Fe is Fe^{2+}. ALIA dredge 115 whole-rock data are from Jackson et al. (2007). Right panel: a conceptual model to explain the trend in the left panel. In this model, two isotopically distinct primary mantle melts are generated (step 1). Each of the endmember melts evolves to a lower Mg#; however, the melt with more radiogenic $^{87}Sr/^{86}Sr$ achieves a lower Mg# than the melt with lower $^{87}Sr/^{86}Sr$ (step 2; see Discussion). Finally, the two different melts mix to produce the trend seen in the left panel of this figure (step 3).

relative to the other ALIA-115-21 plagioclase (mean An $= 54 \pm 2$ [2 SD], $n = 20$; Supplementary Table 4). Of the three crystals from ALIA-115-21, this crystal exhibits the greatest variability in measured $^{87}Sr/^{86}Sr$ (Fig. 5), with $^{87}Sr/^{86}Sr$ values ranging from 0.71982 ± 0.00031 to 0.72192 ± 0.00015 (range $= 2910$ ppm) obtained over two analytical sessions. There is a high-$^{87}Sr/^{86}Sr$ zone near the center of the largest crystal, but the zone is poorly defined owing to relatively few measurements with lower $^{87}Sr/^{86}Sr$ near the periphery of the crystal (Supplementary Fig. 2).

3.2. Geochemical trends recorded in plagioclase

The LASS data define a clear negative relationship between Sr concentration and $^{87}Sr/^{86}Sr$ in the Samoan plagioclase crystals targeted. The data from the crystals separated from ALIA-115-21 define a shallower slope than the data from the ALIA-115-18 crystals, but all share the trend of higher $^{87}Sr/^{86}Sr$ at lower Sr concentration (Fig. 6). The arrays formed by the plagioclase from the two lavas overlap in a common region characterized by high $^{87}Sr/^{86}Sr$. This extreme high-$^{87}Sr/^{86}Sr$ EM2 common component is more radiogenic than any Samoan whole rocks or mineral phases analyzed to date.

The presence of olivine inclusions (c. 20–30 μm) in a domain of a plagioclase that exhibits extremely radiogenic $^{87}Sr/^{86}Sr$ allows us to calculate the Mg# of the melt in equilibrium with the olivine and, by extension, the EM2 endmember sampled by the plagioclase, assuming that the plagioclase and included olivine crystallized from the same portion of homogeneous melt. The composition of the EM2 endmember observed in the plagioclase is relatively evolved: the melt in equilibrium with the olivines included in plagioclase ALIA-115-18-1 has an Mg# of 46.8 ± 0.4 (2 SD). When this composition is plotted with all Samoan lavas from the ALIA-115 dredge, the common component EM2 composition anchors the high-$^{87}Sr/^{86}Sr$, low Mg# inclusions portion of the array (Fig. 7). It is an assumption that the olivine grew from the same melt as the host plagioclase; the olivine may have grown from a more or less evolved melt prior to entrapment. Nonetheless, the calculated Mg# of the olivine inclusion, paired with the $^{87}Sr/^{86}Sr$ of the host plagioclase zone hosting the olivine, results in a melt composition that anchors the high-$^{87}Sr/^{86}Sr$ portion of the whole rock trend in $^{87}Sr/^{86}Sr$-versus-Mg# space in Fig. 7. This supports the hypothesis that the olivine was in equilibrium with the same liquid that crystallized the surrounding plagioclase material.

However, other trace elements analyzed here (e.g., Rb, Ba, Ti, Y, REEs) do not exhibit the same clear relationships with $^{87}Sr/^{86}Sr$; La is shown as an example in Fig. 6. Similarly, the anorthite composition of the plagioclase at each laser spot does not show a relationship with $^{87}Sr/^{86}Sr$ (Fig. 6).

4. Discussion

Two of the six Samoan plagioclase crystals examined here contain the most extreme EM2 signatures ($^{87}Sr/^{86}Sr$ up to 0.7224) ever observed in OIB, and these new, ultrahigh $^{87}Sr/^{86}Sr$ signatures surpass the highest values previously reported in Samoan whole rocks (up to 0.720469) and in magmatic clinopyroxene (up to 0.721630; Jackson et al., 2007). Furthermore, five of the six plagioclase crystals have extreme $^{87}Sr/^{86}Sr$ heterogeneity (> 1500 ppm) that complements the intra-lava $^{87}Sr/^{86}Sr$ heterogeneity measured in plagioclase from mid-ocean ridge basalts (Lange et al., 2013), between olivine-hosted melt inclusions and their host OIB whole rocks (e.g., Harlou et al., 2009; Jackson and Hart, 2006; Reinhard et al., 2016; 2018; Sobolev et al., 2011), and between magmatic clinopyroxene and their host OIB whole rocks (e.g., Hanyu and Nakamura, 2000; Jackson et al., 2009; Hanyu et al., 2011).

The Samoan plagioclase presented here sample an EM2 component with a radiogenic Sr isotopic signature ($^{87}Sr/^{86}Sr = 0.7224$) more extreme than that observed in any mantle-derived oceanic lavas. Below we rule out assimilation and post-eruptive radiogenic ingrowth as processes generating the extreme radiogenic isotopic compositions, and then explore the implications of these new extreme EM2 compositions observed in Samoan plagioclase. In the Supplementary Discussion we evaluate the $^{87}Sr/^{86}Sr$ composition of groundmass in ALIA-115-18 and ALIA-115-21 required by mass balance given the measured $^{87}Sr/^{86}Sr$ compositions of plagioclase

and clinopyroxene phenocrysts. The new extreme EM2 composition recorded in the plagioclase is calculated to be more evolved than any extreme EM2 lava examined to date from the Samoan ALIA-115 dredge, and its radiogenic $^{87}Sr/^{86}Sr$ composition requires that a higher fraction of recycled sediment was added to its source (Jackson et al., 2007).

4.1. Origin of $^{87}Sr/^{86}Sr$ heterogeneity in Samoan plagioclase

The observation of intra-crystal $^{87}Sr/^{86}Sr$ disequilibrium in OIB is one of the salient findings of this study. Therefore, it is important to consider the mechanisms that may have been responsible for generating the $^{87}Sr/^{86}Sr$ heterogeneity in the plagioclase crystals we studied.

Varying degrees of radiogenic ingrowth of ^{87}Sr due to post-eruptive ^{87}Rb decay in the plagioclase cannot generate the extreme $^{87}Sr/^{86}Sr$ heterogeneity in the plagioclase crystals we measured. The lowest (0.00052) and highest (0.0068) measured Rb/Sr ratios from any two ALIA-115 plagioclase spots would lead to $^{87}Sr/^{86}Sr$ differences in the plagioclase of only 2 ppm over the 5.3 Myr (Koppers et al., 2008) since the plagioclase formed. Radiogenic ingrowth is thus not the mechanism responsible for generating $^{87}Sr/^{86}Sr$ variability in these plagioclase crystals.

Assimilation of altered oceanic crust is not likely to have generated the extreme high $^{87}Sr/^{86}Sr$ observed in the Samoan plagioclase (which have $^{87}Sr/^{86}Sr \geq 0.71788$; see Supplementary Table 4), as the $^{87}Sr/^{86}Sr$ signature of altered oceanic crust only rarely achieves $^{87}Sr/^{86}Sr$ values that approach or exceed (e.g., Hauff et al., 2003), the value of seawater ($^{87}Sr/^{86}Sr = 0.709164$; renormalized from Mokadem et al., 2015). Similarly, assimilation of modern sediments is not likely to have generated the extreme $^{87}Sr/^{86}Sr$ signatures observed here: lead is highly enriched in marine sediments (Plank and Langmuir, 1998) compared to oceanic lavas (Willbold and Stracke, 2006), so sediment assimilation would have a disproportionate influence on the Pb isotopic composition of a lava. This is notable because the Samoan EM2 lavas from ALIA dredge 115 form an array in $\Delta^{207}Pb/^{204}Pb$–$\Delta^{208}Pb/^{204}Pb$ space that diverges away from the field formed by modern sediments (Fig. 4 of Jackson et al., 2007), and the extreme EM2 lavas with the highest $^{87}Sr/^{86}Sr$ plot farthest from the field defined by modern sediments in this Pb isotopic space. This observation suggests that the assimilation of modern sediments cannot have generated the enriched $^{87}Sr/^{86}Sr$ signatures in the whole rocks and, by extension, their plagioclase cargo.

One possible mechanism for generating intra-crystal $^{87}Sr/^{86}Sr$ heterogeneity may be mixing of two (or more) isotopically distinct melts. Textural features in the plagioclase support this hypothesis: plagioclase ALIA-115-18-1 (which exhibits the second most extreme degree of intra-crystal $^{87}Sr/^{86}Sr$ variability) has a rounded and resorbed core surrounded by a narrow olivine-bearing zone (Fig. 4), features consistent with magma mixing. The magmatic plagioclase targeted in this study exhibit $^{87}Sr/^{86}Sr$ zoning to varying degrees (Supplementary Fig. 2); the simplest explanation for this observation is that the mixing of isotopically distinct magmas is responsible for the observed isotopic zonation. Furthermore, plagioclase crystals from each lava examined here define a different negatively sloping array in $^{87}Sr/^{86}Sr$–Sr concentration space (Fig. 6), and a key observation is that the arrays overlap at a common high-$^{87}Sr/^{86}Sr$ EM2 component. If mixing was responsible for generating these converging arrays, one or more low-$^{87}Sr/^{86}Sr$ endmembers (with higher Sr concentrations) may have mixed with a common high-$^{87}Sr/^{86}Sr$ component to generate the negatively sloping trend observed in Fig. 6. An important issue to address is the petrological characteristics of the magmas that mixed to generate the trends observed in Fig. 6.

4.2. A new extreme EM2 signature in an evolved melt: evidence for mixing an evolved EM2 magma with less-evolved magmas with lower $^{87}Sr/^{86}Sr$

Fortuitously, olivine (mean Fo $= 74.5 \pm 0.8$, 2 SD) included in plagioclase ALIA-115-18-1—within a zone characterized by high $^{87}Sr/^{86}Sr$—allow us to calculate the Mg# of the EM2 common component magma to be Mg# $= 46.8 \pm 0.4$ (2 SD). Therefore, we infer that the extreme EM2 lava from which the olivine and plagioclase crystallized was relatively evolved. For comparison, a primary melt in equilibrium with Fo_{90} mantle olivine has a Mg# of 73.

This is an important observation because the calculated composition of the EM2 common component lies on an extension of the trend defined by the ALIA-115 whole rocks in $^{87}Sr/^{86}Sr$–Mg# space (Fig. 7): the new extreme EM2 common component has an even lower calculated Mg# and higher measured $^{87}Sr/^{86}Sr$ signature ($^{87}Sr/^{86}Sr = 0.72194 \pm 0.00057$ [2 SD, $n = 4$ spots]) than recorded in ALIA-115 whole-rock lavas. Because all of the lavas that form the compositional array in Fig. 7 are from the same submarine dredge site off the coast of Savai'i island and are presumably petrogenetically linked, we explore a mechanism to explain the observed relationship between $^{87}Sr/^{86}Sr$ and Mg#.

We propose a conceptual model that mirrors the mechanism for formation of the $^{87}Sr/^{86}Sr$–Sr concentration trend illustrated in Fig. 6: binary mixing of an evolved high-$^{87}Sr/^{86}Sr$ EM2 melt and a less evolved low-$^{87}Sr/^{86}Sr$ melt (right panel of Fig. 7). In the model, two geochemically distinct primary mantle melts must be generated, one with low $^{87}Sr/^{86}Sr$ and one with high $^{87}Sr/^{86}Sr$. However, none of the lavas from the ALIA-115 dredge are primary melts (i.e., all lavas from ALIA dredge 115 have a Mg# of ≤ 65), so they have experienced variable degrees of magmatic evolution in the crust prior to eruption. In this dredge, the high-$^{87}Sr/^{86}Sr$ lavas are more evolved than the low-$^{87}Sr/^{86}Sr$ lavas, as indicated in Fig. 7 (left panel). Thus, in the model, a more evolved high-$^{87}Sr/^{86}Sr$ melt and a less evolved low-$^{87}Sr/^{86}Sr$ melt mix in varying proportions, producing an array of intermediate compositions. The ALIA dredge 115 lavas and the extreme EM2 common component sampled by the Samoan plagioclase in this study define a trend in $^{87}Sr/^{86}Sr$–Mg# space that is consistent with this conceptual model (Fig. 7).

This model may also explain why plagioclase $^{86}Sr/^{86}Sr$ is negatively correlated with Sr concentration in Fig. 6: the more-radiogenic mixing endmember is more evolved and is more likely to have experienced greater degrees of plagioclase fractionation. Owing to the compatibility of Sr in plagioclase, the removal of plagioclase from the most-evolved EM2 melts results in residual melt with lower Sr, whereas the less-evolved lavas with lower $^{87}Sr/^{86}Sr$ will have higher Sr concentrations. Although plagioclase fractionation exerts a powerful lever on magmatic Sr concentrations, the concentrations of other trace elements examined in this study will not be as strongly influenced by fractional crystallization of plagioclase (or olivine and clinopyroxene, the other phases identified in ALIA-115 lavas; Koppers et al., 2011). As a result, these other trace elements will not follow the same trends as Sr during magmatic evolution, thereby decoupling $^{86}Sr/^{86}Sr$ from incompatible trace-element signatures other than that of Sr. This mechanism may explain the lack of clear correlations between $^{87}Sr/^{86}Sr$ and other geochemical indicators. Alternatively, the clear relationship between $^{87}Sr/^{86}Sr$ and Sr concentrations—but not other trace-element concentrations (e.g., La in Fig. 6)—may be explained by different cation diffusion rates in plagioclase (e.g., Cherniak, 2003). This is because diffusion may relax original geochemical profiles in the plagioclase to varying degrees during residence in a magma chamber (see Supplementary Discussion), a process that may preserve relationships between $^{87}Sr/^{86}Sr$ and Sr concentration (due to

similar diffusion rates of Sr and Sr-isotopic signatures in plagioclase) while decoupling $^{87}Sr/^{86}Sr$ from other trace elements.

One remaining uncertainty concerns whether the EM2 endmember melt is universally evolved. Although the extreme EM2 mixing endmember sampled by the plagioclase is more evolved than other lavas from the Samoan dredge ALIA-115 locality (Fig. 7), it is not clear whether all EM2 lavas with extreme high $^{87}Sr/^{86}Sr$ ratios should be evolved. Fig. 7 (right panel) posits that a mafic parental melt for the extreme EM2 melt sampled by the ALIA-115-18 and ALIA-115-21 plagioclase existed, but this is uncertain. Mafic extreme EM2 lavas, if they exist, would enhance our understanding of this mantle endmember because they would enable investigation of primary melt phase equilibria and estimates of the temperature and pressure conditions of EM2 mantle melting.

4.3. Generation of an extreme EM2 composition via terrigenous sediment recycling

The high-$^{87}Sr/^{86}Sr$ signature identified in the most extreme EM2 Samoan ALIA-115 lavas has been interpreted to reflect the ancient recycling of upper continental crust-derived sediment subducted into the mantle (Jackson et al., 2007; White and Hofmann, 1982; Workman et al., 2008). Combining trace-element and isotopic constraints, Jackson et al. (2007) estimated that the terrigenous sediment protolith contributing to the Samoan EM2 mantle has an $^{87}Sr/^{86}Sr$ composition of 0.7421 (assuming an upper continental crust Sr concentration of 320 ppm; Rudnick and Gao, 2003). They found that the addition of $\sim 5\%$ of a terrigenous sediment protolith to a depleted peridotite source such as that calculated for the most geochemically depleted lavas in Samoa ($^{87}Sr/^{86}Sr = 0.704650$ and Sr concentration = 28.3 ppm; Jackson et al., 2007), could generate the geochemically enriched trace-element and $^{87}Sr/^{86}Sr$ signatures in the second most extreme EM2 lava from Samoa, ALIA-115-18 (Jackson et al., 2007). Using the same model parameters employed by these authors, we calculate that approximately 7% sediment (i.e., an additional 2%) is required to generate the highest-measured plagioclase $^{87}Sr/^{86}Sr$ value (0.72239 ± 0.00027; 2 SE) reported in this study.

The bulk of marine sediment is derived from the continents: an estimated 76 wt% of marine sediment has a terrigenous origin (Plank and Langmuir, 1998). Thus, subduction of marine sediment contributes a continental signature to the mantle. Over geologic time, significant volumes of sediment have been introduced into the terrestrial mantle; recent sediment subduction flux estimates range from 1.0 $km^3\,a^{-1}$ (von Huene and Scholl, 1991) to 1.65 $km^3\,a^{-1}$ (Clift et al., 2009). We estimate the net mass of sediment that has been added to Earth's mantle over geologic time as follows. We assume a sediment density of 2500 $kg\,m^{-3}$, use the lower sediment subduction flux estimate of von Huene and Scholl (1991), and assume that 90% of all subducting sediment is relaminated to the base of the continents (Hacker et al., 2011). Using a time of 3 Ga (Shirey and Richardson, 2011), we calculate that $7.5 \cdot 10^{20}$ kg of sediment has been added to the convecting mantle. This quantity of sediment is $\sim 0.02\%$ of the mantle by mass (however, if continents were smaller in the past, the total volume of material eroded would have been smaller). Although this quantity of subducted sediment is minor in terms of its mass fraction, it has an outsized geochemical importance: if we assume that the non-sediment portion of the mantle has the primitive composition proposed by McDonough and Sun (1995) and the sediment has a composition like GLOSS (Plank and Langmuir, 1998), then 1.4–1.9% of the most incompatible elements (Rb, Th, U, and K) are hosted in the subducted sediment domain, and 0.3–0.4% of the moderately incompatible elements (e.g., Sr and Nd) are hosted in this domain. This estimate gives a lower limit on the geochemical impact of sediment subduction on the incompatible-element budget of the mantle because the mantle has been partially depleted by the extraction of continental crust and the average composition of the mantle today must therefore be more depleted than the primitive mantle. Assuming a simple model wherein the bulk mantle is 33% DMM and 67% primitive mantle by mass (Workman and Hart, 2005), 1.9–2.7% of the most incompatible elements and 0.5–1.2% of the moderately incompatible elements are hosted in the subducted sediment domain. The degree to which the recycled sediment domain is enriched in incompatible elements depends on the bulk mantle composition that is assumed; however, these estimates illustrate that sediment may play an important role in the geochemical budgets of highly incompatible elements in the mantle.

Although 0.02% of the mass of the mantle may consist of recycled sediment, this sediment component is heterogeneously distributed: approximately 7% of the mantle source of the extreme EM2 domain sampled by the plagioclase in this study consists of recycled sediment based on geochemical constraints. The survival of such sediment-rich domains in the mantle suggests that subducted sediment is not always efficiently mixed in the dynamically convecting mantle, and therefore, geochemical signatures imparted by subducted sediment are not efficiently attenuated. Instead, regions of the mantle can contain relatively high mass fractions of recycled sediment.

There is evidence that subducted sediment is concentrated in certain regions of Earth's mantle. Castillo (1988) found that hotspots exhibiting EM (enriched mantle) signatures are positioned above one of the two near-antipodal large low-shear-velocity provinces (LLSVPs) at the base of the mantle. This finding is supported by a more recent study that investigated the link between the positioning of hotspots relative to LLSVPs and the geochemical enrichment observed in OIB at oceanic hotspots globally (Jackson et al., 2018). If EM domains trace their origins to subducted sediment, the LLSVPs may represent regions that host unusually high concentrations of subducted sediment. LLSVPs may compose up to 7.7% of the mantle by mass (the "majority estimate" of Cottaar and Lekic, 2016), and if most of the subducted sediment is hosted in the LLSVPs, approximately 0.25% of the LLSVPs is composed of subducted sediment. This percentage is higher if the fraction of the mass fraction of the LLSVPs has been overestimated, or if the fraction of sediment that escapes relamination is higher. Nonetheless, the high mass fraction of sediment estimated in the Samoan extreme EM2 source ($\sim 7\%$) is anomalous; it reflects an unusual surviving relic of subducted sediment in the dynamically convecting mantle.

5. Conclusions

We report new $^{87}Sr/^{86}Sr$ measurements of plagioclase in extreme Samoan EM2 lavas. We employ laser-ablation split-stream mass spectrometry (LASS), which permits simultaneous analysis of trace-element concentrations and $^{87}Sr/^{86}Sr$ from the same crystal volume. We measure over 5000 ppm of intra-crystal $^{87}Sr/^{86}Sr$ heterogeneity in two of the six plagioclase samples examined here, which is significantly greater than the long-term analytical reproducibility achieved for a plagioclase reference material (± 350 ppm). Critically, we observe highly radiogenic $^{87}Sr/^{86}Sr$ ratios (up to 0.7224) in plagioclase from two different Samoan EM2 lavas, the highest $^{87}Sr/^{86}Sr$ ratios ever measured in oceanic lavas.

The simultaneous measurement of Sr isotopic and trace-element compositions of the plagioclase reveals a relationship between $^{87}Sr/^{86}Sr$ and Sr concentrations in the six plagioclase crystals analyzed here. Data from the plagioclase crystals overlap at a common enriched EM2 component in $^{87}Sr/^{86}Sr$–Sr concentration space. We interpret $^{87}Sr/^{86}Sr$ heterogeneity in the plagioclase—and the relationship between $^{87}Sr/^{86}Sr$ and Sr concentrations—to reflect

mixing between an evolved extremely enriched EM2 "common component" with at least one component that is less evolved and has less radiogenic $^{87}Sr/^{86}Sr$. We calculate the Mg# of this extreme EM2 common component from the compositions of olivine grains (forsterite content 74.5 ± 0.8, 2 SD) hosted in a high-$^{87}Sr/^{86}Sr$ plagioclase zone that samples the EM2 common component; a melt in equilibrium with the olivines has a Mg# of 46.8 ± 0.4 (2 SD). This new calculated EM2 endmember composition plots on an extension of the negatively sloping array formed by relevant Samoan whole-rock lavas in $^{87}Sr/^{86}Sr$–Mg# space, supporting the contention that extreme EM2 melts in Samoa are relatively evolved.

The discovery of a new extreme EM2 endmember composition provides a new estimate of the amount of recycled terrigenous sediment sampled by an EM2 melt. The elevated $^{87}Sr/^{86}Sr$ recorded in Samoan plagioclase zones requires a high fraction of recycled sediment ($\sim 7\%$) in the Samoan mantle source. This fraction is significantly higher than our estimate for the fraction of Earth's mantle that is likely to be composed of recycled sediment (0.02%). The observation of a new extreme EM2 signature in plagioclase from the Samoan hotspot thus provides new insights on sediment recycling, an important process for generating heterogeneity in Earth's dynamic mantle.

Acknowledgements

We thank Catherine Chauvel and one anonymous reviewer for their constructive reviews that greatly improved this manuscript, and Frédéric Moynier for editorial handling. MAE acknowledges funding from a 2017 summer research fellowship from the UCSB Earth Research Institute. MGJ acknowledges support from National Science Foundation grants EAR-1624840, OCE-1736984 and EAR-1347377. Discussions with Roberta Rudnick and comments on an earlier version of this manuscript were exceedingly helpful. Helpful advice regarding sample preparation and mass spectrometry from Andrew Reinhard is gratefully acknowledged. Stan Hart and Hubert Staudigel generously provided samples from the Samoan region for this study. We thank Casey Saenger for donating a portion of modern sclerosponge from Pear Tree Bottom, Jamaica.

Appendix A. Supplementary material

Supplementary material related to this article can be found online at https://doi.org/10.1016/j.epsl.2019.01.040.

References

Castillo, P., 1988. The Dupal anomaly as a trace of the upwelling lower mantle. Nature 336, 667–670. https://doi.org/10.1038/336667a0.

Cherniak, D.J., 2003. REE diffusion in feldspar. Chem. Geol. 193, 25–41. https://doi.org/10.1016/S0009-2541(02)00246-2.

Christensen, J.N., Halliday, A.N., Lee, D.-C., Hall, C.M., 1995. In situ Sr isotopic analysis by laser ablation. Earth Planet. Sci. Lett. 136, 79–85.

Clift, P.D., Vannucchi, P., Morgan, J.P., 2009. Crustal redistribution, crust-mantle recycling and Phanerozoic evolution of the continental crust. Earth-Sci. Rev. 97, 80–104. https://doi.org/10.1016/j.earscirev.2009.10.003.

Cottaar, S., Lekic, V., 2016. Morphology of seismically slow lower-mantle structures. Geophys. J. Int. 207, 1122–1136. https://doi.org/10.1093/gji/ggw324.

Davidson, J.P., Tepley, F.J., 1997. Recharge in volcanic systems: evidence from isotope profiles of phenocrysts. Science 80 (275), 826–829. https://doi.org/10.1126/science.275.5301.826.

Davidson, J.P., Morgan, D.J., Charlier, B.L.A., Harlou, R., Hora, J.M., 2007. Microsampling and isotopic analysis of igneous rocks: implications for the study of magmatic systems. Annu. Rev. Earth Planet. Sci. 35, 273–311. https://doi.org/10.1146/annurev.earth.35.031306.1402110084-6597/07/0530-0273$20.00.

Font, L., Davidson, J.P., Pearson, D.G., Nowell, G.M., Jerram, D.A., Ottley, C.J., 2008. Sr and Pb isotope micro-analysis of plagioclase crystals from skye lavas: an insight into open-system processes in a flood basalt province. J. Petrol. 49, 1449–1471. https://doi.org/10.1093/petrology/egn032.

Garapić, G., Jackson, M.G., Hauri, E.H., Hart, S.R., Farley, K.A., Blusztajn, J.S., Woodhead, J.D., 2015. A radiogenic isotopic (He–Sr–Nd–Pb–Os) study of lavas from the Pitcairn hotspot: implications for the origin of EM-1 (enriched mantle 1). Lithos 228–229, 1–11. https://doi.org/10.1016/j.lithos.2015.04.010.

Gast, P.W., Tilton, G.R., Hedge, C., 1964. Isotopic composition of lead and strontium from ascension and Gough Islands. Science 80 (145), 1181–1185.

Hacker, B.R., Kelemen, P.B., Behn, M.D., 2011. Differentiation of the continental crust by relamination. Earth Planet. Sci. Lett. 307, 501–516. https://doi.org/10.1016/j.epsl.2011.05.024.

Hanyu, T., Nakamura, E., 2000. Constraints on HIMU and EM by Sr and Nd isotopes re-examined. Earth Planets Space 52, 61–70. https://doi.org/10.1186/BF03351614.

Hanyu, T., Tatsumi, Y., Senda, R., Miyazaki, T., Chang, Q., Hirahara, Y., Takahashi, T., Kawabata, H., Suzuki, K., Kimura, J.I., Nakai, S., 2011. Geochemical characteristics and origin of the HIMU reservoir: a possible mantle plume source in the lower mantle. Geochem. Geophys. Geosyst. 12, 1–30. https://doi.org/10.1029/2010GC003252.

Harlou, R., Pearson, D.G., Nowell, G.M., Ottley, C.J., Davidson, J.P., 2009. Combined Sr isotope and trace element analysis of melt inclusions at sub-ng levels using micro-milling, TIMS and ICPMS. Chem. Geol. 260, 254–268. https://doi.org/10.1016/j.chemgeo.2008.12.020.

Hart, S.R., Schilling, J.-G., Powell, J.L., 1973. Basalts from Iceland and along the Reykjanes ridge: Sr isotope geochemistry. Nature 246, 104–107. https://doi.org/10.1038/10.1038/physci246104a0.

Hauff, F., Hoernle, K., Schmidt, A., 2003. Sr–Nd–Pb composition of Mesozoic Pacific oceanic crust (site 1149 and 801, ODP leg 185): implications for alteration of ocean crust and the input into the Izu–Bonin–Mariana subduction system. Geochem. Geophys. Geosyst. 4. https://doi.org/10.1029/2002GC000421.

Hofmann, A.W., 1997. Mantle geochemistry: the message from oceanic volcanism. Nature 385, 219–229.

Jackson, M.G., Hart, S.R., 2006. Strontium isotopes in melt inclusions from Samoan basalts: implications for heterogeneity in the Samoan plume. Earth Planet. Sci. Lett. 245, 260–277. https://doi.org/10.1016/j.epsl.2006.02.040.

Jackson, M.G., Hart, S.R., Koppers, A.A.P., Staudigel, H., Konter, J., Blusztajn, J., Kurz, M., Russell, J.A., 2007. The return of subducted continental crust in Samoan lavas. Nature 448, 684–687. https://doi.org/10.1038/nature06048.

Jackson, M.G., Hart, S.R., Shimizu, N., Blusztajn, J.S., 2009. The $^{87}Sr/^{86}Sr$ and $^{143}Nd/^{144}Nd$ disequilibrium between Polynesian hot spot lavas and the clinopyroxenes they host: evidence complementing isotopic disequilibrium in melt inclusions. Geochem. Geophys. Geosyst. 10. https://doi.org/10.1029/2008GC002324.

Jackson, M.G., Becker, T.W., Konter, J.G., 2018. Geochemistry and distribution of recycled domains in the mantle inferred from Nd and Pb isotopes in oceanic hot spots: implications for storage in the large low shear wave velocity provinces. Geochem. Geophys. Geosyst. 9. https://doi.org/10.1029/2018GC007552.

Jochum, K.P., Wilson, S.A., Abouchami, W., Amini, M., Chmeleff, J., Eisenhauer, A., Hegner, E., Iaccheri, L.M., Kieffer, B., Krause, J., Mcdonough, W.F., Mertz-Kraus, R., Raczek, I., Rudnick, R.L., Scholz, D., Steinhoefel, G., Stoll, B., Stracke, A., Tonarini, S., Weis, D., Weis, U., Woodhead, J.D., 2011. GSD-1G and MPI-DING reference glasses for in situ and bulk isotopic determination. Geostand. Geoanal. Res. 35, 193–226. https://doi.org/10.1111/j.1751-908X.2010.00114.x.

Konter, J.G., Storm, L.P., 2014. High precision $^{87}Sr/^{86}Sr$ measurements by MC-ICP-MS, simultaneously solving for Kr interferences and mass-based fractionation. Chem. Geol. 385, 26–34. https://doi.org/10.1016/j.chemgeo.2014.07.009.

Koppers, A.A.P., Russell, J.A., Jackson, M.G., Konter, J., Staudigel, H., Hart, S.R., 2008. Samoa reinstated as a primary hotspot trail. Geology 36, 435–438. https://doi.org/10.1130/G24630A.1.

Koppers, A.A., Russell, J.A., Roberts, J., Jackson, M.G., Konter, J.G., Wright, D.J., Staudigel, H., Hart, S.R., 2011. Age systematics of two young en echelon Samoan volcanic trails. Geochem. Geophys. Geosyst. 12 (7). https://doi.org/10.1029/2010GC003438.

Kylander-Clark, A.R.C., Hacker, B.R., Cottle, J.M., 2013. Laser-ablation split-stream ICP petrochronology. Chem. Geol. 345, 99–112. https://doi.org/10.1016/j.chemgeo.2013.02.019.

Lange, A.E., Nielsen, R.L., Tepley, F.J., Kent, A.J.R., 2013. Diverse Sr isotope signatures preserved in mid-oceanic-ridge basalt plagioclase. Geology 41, 279–282. https://doi.org/10.1130/G33739.1.

McDonough, W.F., Sun, S.-s., 1995. The chemical composition of the Earth. Chem. Geol. 120, 223–253. https://doi.org/10.1016/0009-2541(94)00140-4.

Miyazaki, T., Hanyu, T., Kimura, J.I., Senda, R., Vaglarov, B.S., Chang, Q., Hirahara, Y., Takahashi, T., Kawabata, H., Sato, T., 2018. Clinopyroxene and bulk rock Sr–Nd–Hf–Pb isotope compositions of Raivavae ocean island basalts: does clinopyroxene record early stage magma chamber processes? Chem. Geol. 482, 18–31. https://doi.org/10.1016/j.chemgeo.2017.12.015.

Mokadem, F., Parkinson, I.J., Hathorne, E.C., Anand, P., Allen, J.T., Burton, K.W., 2015. High-precision radiogenic strontium isotope measurements of the modern and glacial ocean: limits on glacial-interglacial variations in continental weathering. Earth Planet. Sci. Lett. 415, 111–120. https://doi.org/10.1016/j.epsl.2015.01.036.

Paul, B., Woodhead, J.D., Hergt, J., Danyushevsky, L., Kunihiro, T., Nakamura, E., 2011. Melt inclusion Pb-isotope analysis by LA-MC-ICPMS: assessment of analytical performance and application to OIB genesis. Chem. Geol. 289, 210–223. https://doi.org/10.1016/j.chemgeo.2011.08.005.

Plank, T., Langmuir, C.H., 1998. The chemical composition of subducting sediment and its consequences for the crust and mantle. Chem. Geol. 145, 325–394. https://doi.org/10.1016/S0009-2541(97)00150-2.

Ramos, F.C., Wolff, J.a., Tollstrup, D.L., 2005. Sr isotope disequilibrium in Columbia river flood basalts: evidence for rapid shallow-level open-system processes. Geology 33, 457. https://doi.org/10.1130/G21512.1.

Reinhard, A.A., Jackson, M.G., Harvey, J., Brown, C., Koornneef, J.M., 2016. Extreme differences in $^{87}Sr/^{86}Sr$ between Samoan lavas and the magmatic olivines they host: evidence for highly heterogeneous $^{87}Sr/^{86}Sr$ in the magmatic plumbing system sourcing a single lava. Chem. Geol. 439, 120–131. https://doi.org/10.1016/j.chemgeo.2016.05.017.

Reinhard, A.A., Jackson, M.G., Koornneef, J.M., Rose-Koga, E.F., Blusztajn, J., Konter, J.G., Koga, K.T., Wallace, P.J., Harvey, J., 2018. Sr and Nd isotopic compositions of individual olivine-hosted melt inclusions from Hawai'I and Samoa: implications for the origin of isotopic heterogeneity in melt inclusions from OIB lavas. Chem. Geol. 495, 36–49. https://doi.org/10.1016/j.chemgeo.2018.07.034.

Roeder, P.L., Emslie, R.F., 1970. Olivine-liquid equilibrium. Contrib. Mineral. Petrol. 29, 275–289. https://doi.org/10.1007/BF00371276.

Rudnick, R.L., Gao, S., 2003. Composition of the continental crust. In: Treatise on Geochemistry, vol. 1, pp. 1–64.

Saal, A.E., Hart, S.R., Shimizu, N., Hauri, E.H., Layne, G.D., 1998. Pb isotopic variability in melt inclusions from oceanic island basalts. Polyn. Sci. 80 (282), 1481–1484.

Shirey, S.B., Richardson, S.H., 2011. Start of the Wilson cycle at 3 Ga shown by diamonds from subcontinental mantle. Science 80 (333), 434–436. https://doi.org/10.1126/science.1206275.

Sobolev, A.V., Hofmann, A.W., Jochum, K.P., Kuzmin, D.V., Stoll, B., 2011. A young source for the Hawaiian plume. Nature 476, 434–439. https://doi.org/10.1038/nature10321.

Stracke, A., 2012. Earth's heterogeneous mantle: a product of convection-driven interaction between crust and mantle. Chem. Geol. 330–331, 274–299. https://doi.org/10.1016/j.chemgeo.2012.08.007.

von Huene, R., Scholl, D.W., 1991. Observations at convergent margins concerning sediment subduction, erosion, and the growth of continental crust. Rev. Geophys. 29, 279–316. https://doi.org/10.1029/91RG00969.

White, W.M., 2015. Isotopes, DUPAL, LLSVPs, and Anekantavada. Chem. Geol. 419, 10–28. https://doi.org/10.1016/j.chemgeo.2015.09.026.

White, W., Hofmann, A., 1982. Sr and Nd isotope geochemistry of oceanic basalts and mantle evolution. Nature 296, 821–825. https://doi.org/10.1038/296821a0.

Willbold, M., Stracke, A., 2006. Trace element composition of mantle end-members: implications for recycling of oceanic and upper and lower continental crust. Geochem. Geophys. Geosyst. 7, 1–30. https://doi.org/10.1029/2005GC001005.

Workman, R.K., Hart, S.R., 2005. Major and trace element composition of the depleted MORB mantle (DMM). Earth Planet. Sci. Lett. 231, 53–72. https://doi.org/10.1016/j.epsl.2004.12.005.

Workman, R.K., Hart, S.R., Jackson, M., Regelous, M., Farley, K.A., Blusztajn, J., Kurz, M., Staudigel, H., 2004. Recycled metasomatized lithosphere as the origin of the enriched mantle II (EM2) end-member: evidence from the Samoan volcanic chain. Geochem. Geophys. Geosyst. 5, 1–44. https://doi.org/10.1029/2003GC000623.

Workman, R.K., Eiler, J.M., Hart, S.R., Jackson, M.G., 2008. Oxygen isotopes in Samoan lavas: confirmation of continent recycling. Geology 36, 551–554. https://doi.org/10.1130/G24558A.1.

Yurimoto, H., Kogiso, T., Abe, K., Barsczus, H.G., Utsunomiya, A., Maruyama, S., 2004. Lead isotopic compositions in olivine-hosted melt inclusions from HIMU basalts and possible link to sulfide components. Phys. Earth Planet. Inter. 146, 231–242. https://doi.org/10.1016/j.pepi.2003.08.013.

Zindler, A., Hart, S.R., 1986. Chemical geodynamics. Annu. Rev. Earth Planet. Sci. 14, 493–571. https://doi.org/10.1146/annurev.earth.14.1.493.